Smoothed particle hydrodynamics model for Landau-Lifshitz-Navier-Stokes and advection-diffusion equations

Jannes Kordilla, Wenxiao Pan, and Alexandre Tartakovsky

Citation: The Journal of Chemical Physics **141**, 224112 (2014); doi: 10.1063/1.4902238
View online: http://dx.doi.org/10.1063/1.4902238
View Table of Contents: http://scitation.aip.org/content/aip/journal/jcp/141/22?ver=pdfcov
Published by the AIP Publishing

Smoothed particle hydrodynamics model for Landau-Lifshitz-Navier-Stokes and advection-diffusion equations

Jannes Kordilla,[1,a)] Wenxiao Pan,[2,b)] and Alexandre Tartakovsky[2,c)]
[1]*Geoscientific Centre, University of Göttingen, Göttingen, Germany*
[2]*Computational Mathematics Group, Pacific Northwest National Laboratory, Richland, WA 99352, USA*

(Received 1 July 2014; accepted 10 November 2014; published online 10 December 2014)

We propose a novel smoothed particle hydrodynamics (SPH) discretization of the fully coupled Landau-Lifshitz-Navier-Stokes (LLNS) and stochastic advection-diffusion equations. The accuracy of the SPH solution of the LLNS equations is demonstrated by comparing the scaling of velocity variance and the self-diffusion coefficient with kinetic temperature and particle mass obtained from the SPH simulations and analytical solutions. The spatial covariance of pressure and velocity fluctuations is found to be in a good agreement with theoretical models. To validate the accuracy of the SPH method for coupled LLNS and advection-diffusion equations, we simulate the interface between two miscible fluids. We study formation of the so-called "giant fluctuations" of the front between light and heavy fluids with and without gravity, where the light fluid lies on the top of the heavy fluid. We find that the power spectra of the simulated concentration field are in good agreement with the experiments and analytical solutions. In the absence of gravity, the power spectra decay as the power −4 of the wavenumber—except for small wavenumbers that diverge from this power law behavior due to the effect of finite domain size. Gravity suppresses the fluctuations, resulting in much weaker dependence of the power spectra on the wavenumber. Finally, the model is used to study the effect of thermal fluctuation on the Rayleigh-Taylor instability, an unstable dynamics of the front between a heavy fluid overlaying a light fluid. The front dynamics is shown to agree well with the analytical solutions. © *2014 AIP Publishing LLC*. [http://dx.doi.org/10.1063/1.4902238]

I. INTRODUCTION

In the presence of a macroscopic concentration gradient (e.g., the concentration gradient across the front separating two miscible fluids), non-equilibrium systems are known to relax to an equilibrated state via diffusion.[1,2] On macroscopic scales, diffusion is often approximated by Fick's law.[3] However, on mesoscopic or molecular scales, thermal fluctuations become a significant part of the hydrodynamics and greatly influence mixing. Thermal fluctuations may have a significant impact on miscible fluids close to a hydrodynamic instability, such as Rayleigh-Taylor and Kelvin-Helmholtz instabilities. Fluctuations may also have significant qualitative impact even on hydrodynamically stable miscible systems. For example, thermal fluctuations produce anomalously large fluctuations of the front separating two miscible fluids (with a light fluid overlaying a heavy fluid). Such fluctuations are often called "giant fluctuations" to emphasize the fact that they can be observed by the naked eye.[4–6]

The fluctuations of thermodynamic quantities have been extensively studied in the context of Brownian motion. Einstein[7] and Smoluchowski[8] demonstrated that diffusion resulting from the thermal fluctuations and random movement of a particle in a fluid has the same origin as the dissipative drag forces exerted on the particle by the fluid. Later, this relationship was quantitatively described by the fluctuation-dissipation theorem.[9]

To capture the effect of thermal fluctuations on fluid flow at the hydrodynamic scale, Landau and Lifshitz[10] proposed a stochastic form of the Navier-Stokes (NS) equations that is commonly referred to as Landau-Lifshitz-Navier-Stokes (LLNS) equations. In LLNS equations, a random stress is added to the NS equations, and the strength of the random stress is related to the viscous stress via the fluctuation-dissipation theorem. Similarly, a random mass flux is added into the advection-diffusion equation to consistently include the effect of thermal fluctuations on Fickian diffusion. The most common numerical techniques for directly solving LLNS and stochastic diffusion equations are based on the finite-volume method.[11–14] Stochastic Lattice Boltzmann models[15] and smoothed dissipative particle dynamics (SDPD)[16,17] have been used to model fluid flow in the presence of fluctuations, but these methods have not been derived via the direct discretization of LLNS equations. For example, SDPD is obtained by adding a random force into the smoothed particle hydrodynamics (SPH) discretization of the (deterministic) NS equations and relating the magnitude of the random force to the viscous SPH force via the GENERIC framework.[18–20] Moreover, these methods have not been used to solve stochastic diffusion equations coupled with LLNS equations.

Here, we use the SPH method to solve stochastic partial differential equations, including LLNS and advection-diffusion equations. The SPH method provides an alternative

[a)]jkordil@gwdg.de
[b)]Wenxiao.Pan@pnnl.gov
[c)]alexandre.tartakovsky@pnnl.gov

to SDPD for introducing fluctuations in the SPH flow equations. It also provides a consistent framework for discretizing other stochastic conservation equations. We demonstrate the accuracy of the SPH solution of the LLNS equations by comparing statistics of the fluctuations of pressure and velocity with analytical solutions. The accuracy of the stochastic advection-diffusion equation solution is verified by comparing moments of a conservative tracer with the analytical solution. Finally, we use the coupled LLNS and advection-diffusion equations to study the effect of fluctuations on the diffusive front in the absence and presence of gravity. We analyze the spatial correlation of the diffusive front geometry and compare the results with theoretical predictions. Furthermore, the classical Rayleigh-Taylor instability is simulated to verify the accuracy of the stochastic SPH model.

II. STOCHASTIC FLOW AND TRANSPORT EQUATIONS

We study the isothermal stochastic NS equations including the continuity equation

$$\frac{D\rho}{Dt} = -\rho(\nabla \cdot \boldsymbol{v}), \tag{1}$$

the momentum conservation equation

$$\frac{D\boldsymbol{v}}{Dt} = -\frac{1}{\rho}\nabla P + \frac{1}{\rho}\nabla \cdot \boldsymbol{\tau} + \boldsymbol{g} + \frac{1}{\rho}\nabla \cdot \boldsymbol{s}, \tag{2}$$

and the stochastic advection-diffusion equation

$$\frac{DC}{Dt} = \frac{1}{\rho}\nabla \cdot (\rho D^F \nabla C) + \frac{1}{\rho}\nabla \cdot \boldsymbol{J}. \tag{3}$$

Here, $D/Dt = \partial/\partial t + \boldsymbol{v} \cdot \nabla$ is the total derivative, and ρ, $\boldsymbol{v}$, P, and $\boldsymbol{g}$ are the density, velocity, pressure, and body force. D^F is the Fickian diffusion coefficient. The components of the viscous stress $\boldsymbol{\tau}$ are given by

$$\tau^{ik} = \mu\left(\frac{\partial v^i}{\partial x^k} + \frac{\partial v^k}{\partial x^i}\right), \tag{4}$$

where μ is the (shear) viscosity and the bulk viscosity is assumed to be equal to $\frac{2}{3}\mu$. $C = \widetilde{C}/C_{max}$ is the normalized mass fraction of solute, varying from zero to one ($\widetilde{C}$ is the mass fraction, and C_{max} is the maximum mass fraction). In the following, we refer to C as concentration. The fluctuations in velocity and concentration are caused by the random stress tensor

$$\boldsymbol{s} = \sigma\boldsymbol{\xi}, \tag{5}$$

and random flux vector

$$\boldsymbol{J} = \tilde{\sigma}\tilde{\boldsymbol{\xi}}, \tag{6}$$

where $\boldsymbol{\xi}$ is a random symmetric tensor, $\tilde{\boldsymbol{\xi}}$ is a random vector (whose components are random Gaussian variables), and σ and $\tilde{\sigma}$ are the strengths of the corresponding noises. The random stress is related to the viscous stress by the fluctuation-dissipation theorem.[10] For incompressible and low-compressible fluids, the covariance of the stress components is

$$\begin{aligned}\overline{s^{ik}(\mathbf{r}_1, t_1)s^{lm}(\mathbf{r}_2, t_2)} &= \sigma^2\delta(\mathbf{r}_1 - \mathbf{r}_2)\delta(t_1 - t_2)\\ \sigma^2 &= 2\mu k_B T\delta^{im}\delta^{kl},\end{aligned} \tag{7}$$

where k_B is the Boltzmann constant, T denotes the temperature, $\delta(z)$ is the Dirac delta function, and δ^{ij} is the Kronecker delta function. The fluctuation-dissipation theorem is also used to relate the random flux $\boldsymbol{J}$ to the diffusion term[21]

$$\begin{aligned}\overline{J^i(\mathbf{r}_1, t_1)J^j(\mathbf{r}_2, t_2)} &= \tilde{\sigma}^2\delta(\mathbf{r}_1 - \mathbf{r}_2)\delta(t_1 - t_2)\\ \tilde{\sigma}^2 &= 2m_m DC(1 - C)\rho\delta^{ij},\end{aligned} \tag{8}$$

where m_m is the mass of a single solvent molecule. In general, the fluid density and viscosity are functions of the solute concentration C.

III. SPH DISCRETIZATION

Numerical discretization of the stochastic partial differential equations using SPH is based on the following identity for a continuous field $f(\boldsymbol{r})$ defined on a domain Ω:

$$f(\boldsymbol{r}) = \int_\Omega f(\boldsymbol{r}')\delta(\boldsymbol{r} - \boldsymbol{r}')d\boldsymbol{r}'. \tag{9}$$

To construct a numerical scheme, the δ function is approximated with a smooth kernel function W yielding the *integral* approximation of $f(\boldsymbol{r})$[22]

$$\langle f(\boldsymbol{r})\rangle = \int_\Omega f(\boldsymbol{r}')W(|\boldsymbol{r} - \boldsymbol{r}'|, h)d\boldsymbol{r}'. \tag{10}$$

The kernel $W(|\boldsymbol{r} - \boldsymbol{r}'|, h)$ satisfies: (1) the normalization condition

$$\int_\Omega W(|\boldsymbol{r} - \boldsymbol{r}'|, h)d\boldsymbol{r}' = 1; \tag{11}$$

(2) has compact support h, $W(r > h, h) = 0$; and (3) in the limit of $h \to 0$, W approaches the Dirac delta function

$$\lim_{h\to 0} W(|\boldsymbol{r} - \boldsymbol{r}'|, h) = \delta(\boldsymbol{r} - \boldsymbol{r}'). \tag{12}$$

In this work, we use a fourth-order weighting function to describe W[23]

$$W(|\boldsymbol{r}|, h) = \frac{\alpha_k}{h^3}\begin{cases}\left(3 - \frac{3|\boldsymbol{r}|}{h}\right)^5 - 6\left(2 - \frac{3|\boldsymbol{r}|}{h}\right)^5 + 15\left(1 - \frac{3|\boldsymbol{r}|}{h}\right)^5 & 0 \le |\boldsymbol{r}| < \frac{1}{3}h,\\ \left(3 - \frac{3|\boldsymbol{r}|}{h}\right)^5 - 6\left(2 - \frac{3|\boldsymbol{r}|}{h}\right)^5 & \frac{1}{3}h \le |\boldsymbol{r}| < \frac{2}{3}h,\\ \left(3 - \frac{3|\boldsymbol{r}|}{h}\right)^5 & \frac{2}{3}h \le |\boldsymbol{r}| < h,\\ 0 & |\boldsymbol{r}| > h,\end{cases} \tag{13}$$

where $\alpha_k = 81/(359\pi)$ is the normalization constant.

Next, Ω is discretized with N points (that are usually referred to as "particles") with positions $\boldsymbol{r}_j$ ($j = 1, \ldots, N$), and the integral in Eq. (10) is approximated as a sum to obtain the *discrete* approximation $\langle\langle f(\boldsymbol{r})\rangle\rangle$ of $f(\boldsymbol{r})$

$$\langle\langle f(\boldsymbol{r})\rangle\rangle = \sum_{j=1}^{N} f_j W(|\boldsymbol{r} - \boldsymbol{r}_j|, h)\Delta V_j = \sum_{j=1}^{N} \frac{1}{n_j} f_j W(|\boldsymbol{r} - \boldsymbol{r}_j|, h), \tag{14}$$

where $f(\boldsymbol{r}_j) = f_j$, $\Delta V_j = \frac{m_j}{\rho_j}$ is the volume associated with particle j, m_j is the prescribed mass of particle j, ρ_j is the mass density of the fluid at position $\boldsymbol{r}_j$, and $n_j = \frac{\rho_j}{m_j}$ is the number density. Equation (14) computes spatial derivatives of $\langle\langle f(\boldsymbol{r})\rangle\rangle$ exactly as

$$\nabla\langle\langle f(\boldsymbol{r})\rangle\rangle = \sum_{j=1}^{N} \frac{f_j}{n_j} \nabla W(|\boldsymbol{r} - \boldsymbol{r}_j|, h), \tag{15}$$

where $\nabla W(|\boldsymbol{r} - \boldsymbol{r}_j|, h)$ can be found analytically.

If the particles are uniformly distributed (e.g., located on a regular lattice with the lattice size Δ), then the particle number density can be found exactly as $n_j = \Delta^{-d}$, where d is the number of spatial dimensions. In the Lagrangian SPH framework, the particles are advected with the fluid velocity and become disordered. For a non-uniform particle distribution, the particle number density can be approximately found from Eq. (14) with $f_i = n_i$ as

$$\langle\langle n_i\rangle\rangle = \sum_{j=1}^{N} W(|\boldsymbol{r} - \boldsymbol{r}_j|, h). \tag{16}$$

Alternatively, $n_i = \rho_i/m_i$ can be found from the continuity equation. To simplify the notation, we will drop double brackets in the following derivations.

Using Eqs. (14) and (15), an SPH discretization of the LLNS Eqs. (1) and (2) can be obtained as[10,24,25]

$$\frac{D(m_i \mathbf{v}_i)}{Dt} = \boldsymbol{F}_i, \tag{17}$$

$$\boldsymbol{F}_i = -\sum_{j=1}^{N} \left(\frac{P_j}{n_j^2} + \frac{P_i}{n_i^2}\right) \frac{\mathbf{r}_{ij}}{r_{ij}} \frac{dW(r_{ij}, h)}{dr_{ij}} + \sum_{j=1}^{N} \frac{5(\mu_i + \mu_j)}{n_i n_j} \frac{(\mathbf{v}_{ij} \cdot \mathbf{r}_{ij})}{r_{ij}^2} \frac{\mathbf{r}_{ij}}{r_{ij}} \frac{dW(r_{ij}, h)}{dr_{ij}} + m_i \boldsymbol{g} + \sum_{j=1}^{N} \left(\frac{\boldsymbol{s}_j}{n_j^2} + \frac{\boldsymbol{s}_i}{n_i^2}\right) \cdot \frac{\mathbf{r}_{ij}}{r_{ij}} \frac{dW(r_{ij}, h)}{dr_{ij}}. \tag{18}$$

Following Tartakovsky and Meakin[23] and Zhu and Fox,[26] a numerical discretization of the convection-diffusion equation is obtained as

$$\frac{D(m_i C_i)}{Dt} = \sum_{j=1}^{N} \frac{(D_i^F m_i n_i + D_j^F m_j n_j)(C_i - C_j)}{n_i n_j} \left(\frac{1}{r_{ij}} \frac{dW(r_{ij}, h)}{dr_{ij}}\right) + \sum_{j=1}^{N} \left(\frac{\boldsymbol{J}_j}{n_j^2} + \frac{\boldsymbol{J}_i}{n_i^2}\right) \cdot \frac{\mathbf{r}_{ij}}{r_{ij}} \frac{dW(r_{ij}, h)}{dr_{ij}}. \tag{19}$$

The particle positions are evolved in time according to

$$\frac{d\boldsymbol{r}_i}{dt} = \boldsymbol{v}_i. \tag{20}$$

Here, $\boldsymbol{v}_i$ is the velocity of particle i, t is time, P_i is the fluid pressure at $\boldsymbol{r}_i$, $\boldsymbol{s}_i$ is the random stress at $\boldsymbol{r}_i$, $r_{ij} = |\boldsymbol{r}_{ij}|$, $\boldsymbol{r}_{ij} = \boldsymbol{r}_i - \boldsymbol{r}_j$, and $\boldsymbol{v}_{ij} = \boldsymbol{v}_i - \boldsymbol{v}_j$. For computational efficiency, we set h to unity and locate particles within the interaction range using a common link-list approach with an underlying cubic-lattice, size $h = 1.0$.

To close the system of SPH equations, we employ the ideal gas equation of state (EOS) in the form

$$P_i = c^2 m_i n_i, \tag{21}$$

where c is the artificial speed of sound, which is chosen so the desired compressibility of the system is obtained. Depending on the application, this EOS is often applied to incompressible systems,[27–29] where a choice of c, based on dimensionless analysis,[27,30] can yield the quasi-incompressible approximation of an incompressible fluid.

In general, m_i and μ_i depend on C_i. In SPH, the mass fraction can be defined as $\widetilde{C}_i = m_i^s/m_i = m_i^s/(m_i^0 + m_i^s)$, where m_i is the total mass of particle i (mass of the solution carried by particle i), m_i^s is the mass of solute, and m_i^0 is the mass of solvent carried by particle i. Then, the dependence of m_i on C_i can be expressed as

$$m_i = m_i^0 + m_i \widetilde{C}_i = m_i^0 + m_i C_{max} C_i. \tag{22}$$

In the following, we assume that m_i^0 is constant (i.e., does not change as result of diffusion), $\widetilde{C} \ll 1$ (dilute solution), the mass of solute carried by particle i is $m_i^s = m_i^0 \widetilde{C}_i$, and

$$m_i = m_i^0 + \kappa C_i, \tag{23}$$

where $\kappa = m_i^0 C_{max}$ is a constant. Then, Eq. (19) can be linearized as

$$\frac{DC_i}{Dt} = G_i,$$

$$G_i = \frac{1}{m_i^0} \sum_{j=1}^{N} \frac{(D_i^F m_i n_i + D_j^F m_j n_j)(C_i - C_j)}{n_i n_j} \times \left(\frac{1}{r_{ij}} \frac{dW(r_{ij}, h)}{dr_{ij}}\right) + \frac{1}{m_i^0} \sum_{j=1}^{N} \left(\frac{\boldsymbol{J}_j}{n_j^2} + \frac{\boldsymbol{J}_i}{n_i^2}\right) \cdot \frac{\mathbf{r}_{ij}}{r_{ij}} \frac{dW(r_{ij}, h)}{dr_{ij}}. \tag{24}$$

For the sake of simplicity, we neglect the dependence of viscosity on the fluid compositions.

In SPH, the fluid domain is discretized with fluid particles with volume $\Delta V_i = 1/n_i$, and time integration is done with time step Δt. Therefore, we can write the *lm*-component of the random stress tensor at $\boldsymbol{r}_i$ as

$$s_i^{lm} = \sqrt{\frac{2\mu k_B T \delta^{lm}}{\Delta V_i \Delta t}}\xi_i^{lm} = \sqrt{\frac{2\mu k_B T \delta^{lm} n_i}{\Delta t}}\xi_i^{lm}, \tag{25}$$

where ξ_i^{lm} is a unitless random number from a uniform or normal distribution with a unit variance. No summation over repeating indices is assumed in Eq. (25). Similarly, the *l*-component of the random flux can be written as

$$J_i^l = \sqrt{\frac{2m_m D^F C(1-C)\rho_i}{\Delta V_i \Delta t}}\tilde{\xi}_i^l = \sqrt{\frac{2m_m m_i D^F C(1-C) n_i^2}{\Delta t}}\tilde{\xi}_i^l, \tag{26}$$

where $\tilde{\xi}_i^l$ is a unitless random number from a uniform or normal distribution with a unit variance.

To maintain the kinetic energy of the modeled system independent of resolution (number of particles) and recover the appropriate scaling behavior of velocity fluctuations with temperature, we follow the work of Füchslin *et al.*[31] and introduce scaling of the Boltzmann constant, k_B. Consider a fluid system modeled with two different resolutions corresponding to N^* and N number of particles, respectively, where N^* is the number of particles in the referenced model. We assume that the Boltzmann constant in the system with N^* particles is kB and $\tilde{k}B$ in the system with N particles. Equating the total kinetic energy of the models with these two resolutions leads to $\frac{3}{2}N^* k_B T = \frac{3}{2}N\tilde{k}_B T$. Noting that the average particle volume is inversely proportional to the number of particles, we arrive at the scaling law

$$\widetilde{k}_B = \frac{V}{V^*}k_B, \tag{27}$$

where V is the average volume of particles in the system with N particles and V^* is the average volume of particles in the system with N^* particles. Next, we rewrite Eq. (25) as

$$s_i^{lm} = \sqrt{\frac{2\mu V^* \widetilde{k}_B T \delta^{lm} n_i}{V_i \Delta t}}\xi_i^{lm}, \tag{28}$$

where we replace V with $V_i = 1/n_i$, the volume of particle i. We numerically determined that the correct hydrodynamics is obtained with $V^* = 2h^3$. Therefore, we set the expression for stress to

$$s_i^{lm} = \sqrt{\frac{4h^3 \mu T^* \delta^{lm} n_i^2}{\Delta t}}\xi_i^{lm}, \tag{29}$$

where $T^* = \widetilde{k}_B T$.

To integrate the SPH Eqs. (17) and (20), an explicit "velocity-Verlet" algorithm[32] with adaptive time stepping is employed

$$\boldsymbol{r}_i(t+\Delta t) = \boldsymbol{r}_i(t) + \Delta t \boldsymbol{v}_i(t) + 0.5\Delta t^2 \boldsymbol{F}_i(t)/m_i, \tag{30}$$

$$C_i(t+\Delta t) = C_i(t) + 0.5\Delta t[G_i(t) + G_i(t+\Delta t)], \tag{31}$$

$$m_i(t+\Delta t) = m_i^s + \kappa C_i(t+\Delta t), \tag{32}$$

$$\boldsymbol{v}_i(t+\Delta t) = \frac{m_i(t)\boldsymbol{v}_i(t) + 0.5\Delta t[\boldsymbol{F}_i(t) + \boldsymbol{F}_i(t+\Delta t)]}{m_i(t+\Delta t)}, \tag{33}$$

where $\boldsymbol{F}_i(t+\Delta t)$ is computed as a function of $\boldsymbol{r}_j(t+\Delta t)$ and $\boldsymbol{v}_j(t)$ ($j = 1, \ldots, N$). At each time step, the solution's stability is ensured by satisfying the time step constraints[27,28]

$$\Delta t = \min\left[\epsilon \min_i \frac{h}{3|\boldsymbol{v}_i|}, \epsilon \min_i \sqrt{\frac{h}{3|\boldsymbol{a}_i|}}, \epsilon \min_i \frac{\rho_i h^2}{9\mu}, \epsilon \min_i \frac{h^2}{9D}\right], \tag{34}$$

where $|\cdot|$ is the magnitude of a vector, $\Delta t = (\Delta t_k + \Delta t_{k-1})/2$ with subscript k denotes the current and previous time step, ϵ is a factor (in general, less then one) needed to ensure proper convergence behavior in the mesoscopic SPH model, and $a_i = d\boldsymbol{v}_i/dt$.

IV. SMOOTHED DISSIPATIVE PARTICLE HYDRODYNAMICS

In the SDPD method, the stochastic flow equation is obtained by applying the fluctuation-dissipation theorem directly to the discretized momentum conservation equation

$$\frac{D(m_i \mathbf{v}_i)}{Dt} = -\sum_{j=1}^{N}\left(\frac{P_j}{n_j^2} + \frac{P_i}{n_i^2}\right)\frac{\mathbf{r}_{ij}}{r_{ij}}\frac{dW(r_{ij},h)}{dr_{ij}} + \sum_{j=1}^{N}\frac{5(\mu_i+\mu_j)}{n_i n_j}\frac{(\mathbf{v}_{ij}\cdot\mathbf{r}_{ij})}{r_{ij}^2}\frac{\mathbf{r}_{ij}}{r_{ij}}\frac{dW(r_{ij},h)}{dr_{ij}} + m_i\boldsymbol{g} + \sum_{j=1}^{N}\mathbf{F}_{ij}^S. \tag{35}$$

Specifically, the fluctuation dissipation theorem is used to relate the stochastic force $\mathbf{F}_{ij}^S$ to the viscous (dissipative) force

$$\boldsymbol{F}_{ij}^{(visc)} = \frac{5(\mu_i+\mu_j)}{n_i n_j}\frac{(\mathbf{v}_{ij}\cdot\mathbf{r}_{ij})}{r_{ij}^2}\frac{\mathbf{r}_{ij}}{r_{ij}}\frac{dW(r_{ij},h)}{dr_{ij}} \tag{36}$$

as

$$F_{ij}^{S,l} = B_{ij}\frac{r_{ij}^l}{|r_{ij}|}\frac{\tilde{\zeta}_{ij}^l}{\sqrt{dt}}, \tag{37}$$

where

$$B_{ij} = \sqrt{-2\widetilde{k}_B T \frac{5(\mu_i+\mu_j)}{n_i n_j}\frac{1}{r_{ij}}\frac{dW(r_{ij},h)}{dr_{ij}}} \tag{38}$$

and $\tilde{\zeta}_{ij}^l = \tilde{\zeta}_{ji}^l$ is a random number from a Gaussian distribution with zero mean and unity variance and superscript l denotes the l-component of the vectors.

V. VALIDATION OF THE SPH METHOD FOR LLNS EQUATIONS

We study the accuracy of the SPH solution of the LLNS equations by comparing thermodynamic quantities, such as

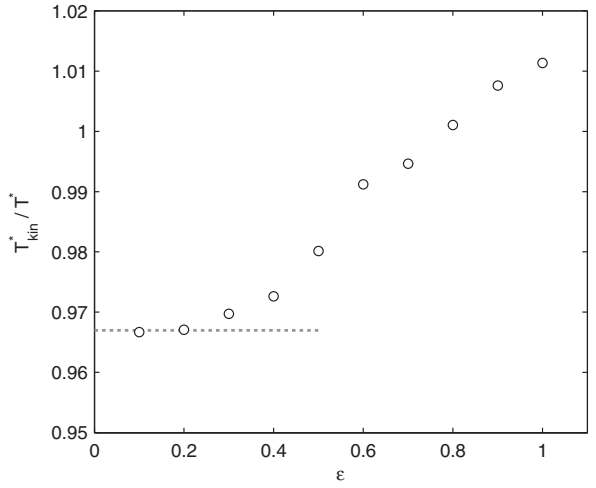

FIG. 1. Effect of time step reduction factor ϵ on the deviation of the system temperature from the prescribed temperature. $T^* = 0.01$, $n_{eq} = 20$, $\rho_0 = 30$, $m = 1.5$, and $\mu = 10$. Convergence is reached for $\epsilon \leq 0.25$.

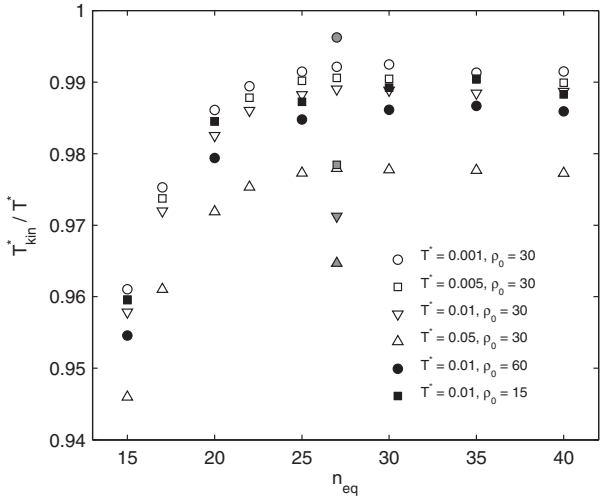

FIG. 2. Scaling of kinetic system temperature with changes in resolution and changes of the mass density ρ_0. Here, $\mu = 10$, and $\epsilon = 0.5$. Convergence is reached for $n_{eq} \geq 20$. Gray markers correspond to the kinetic temperatures for the SDPD implementation of the stochastic stress at $n_{eq} = 27$.

kinetic temperature and velocity variance obtained from the SPH simulations and analytical solutions.

A. Convergence of the SPH solution of LLNS equations

First, we study the convergence behavior of the SPH solution of stochastic NS equations with respect to time step and spatial resolution.

Figure 1 shows the dependence of T^*_{kin}/T^* on the time step. The normalized kinetic temperature $T^*_{kin} = \widetilde{k}_B T_{kin}$ is computed as

$$T^*_{kin} = \frac{1}{3}\sum_{i=1}^{N} m_i\left(\delta v^2_{x,i} + \delta v^2_{y,i} + \delta v^2_{z,i}\right), \tag{39}$$

where $\delta v_{k,i} = v_{k,i} - \langle v_k \rangle$ ($k = x, y, z$) are the fluctuations of k-component of the velocity of particle i around the mean velocity in k-direction, $\langle v_k \rangle = \frac{1}{N}\sum_{i=1}^{N} v_{k,i}$. In our simulations, there are no sources of energy other than random fluctuations, and the kinetic temperature of the system should theoretically be equal to the temperature prescribed in Eq. (7), i.e., T^*_{kin}/T^* should be equal to one. In the simulations shown in Fig. 1, the model domain has the size $L_x = L_y = L_z = 8\,h$ and is periodic in all three directions. The prescribed temperature is $T^* = 0.01$, number density $n_{eq} = 20$, mass density of $\rho_{eq} = n_{eq} m_0 = 30$, mass $m_i = m_0 = 1.5$, and viscosity $\mu = 10$. We found domain size effects to be negligible when $L_x = L_y = L_z \geq 8\,h$. Convergence is reached at about $\epsilon = 0.25$ using the time step criteria in Eq. (34). To keep computation times lower, we set $\epsilon = 0.5$ in all of the following simulations, yielding a difference of about 1% compared to $\epsilon = 0.25$. We note that the kinetic temperature is proportional to the velocity variance. Therefore, Fig. 1 also illustrates that for sufficiently small Δt, the SPH model correctly predicts the velocity variance.

Next, we study the effect of resolution (i.e., n_{eq}) on the accuracy of the SPH model. In Fig. 2, we plot T^*_{kin}/T^* versus the equilibrium density n_{eq}. In the simulations shown in this figure, the equilibrium mass density is kept constant ($\rho_{eq} = 30$), and the mass of the particles is set to $m_i = m_0 = \rho_{eq}/n_{eq}$. It is important to note that the speed of sound should scale with mass as

$$c \sim \sqrt{\frac{k_B T}{m_0}} = \sqrt{\frac{2h^3 \rho_{eq} T^*}{m_0^2}}. \tag{40}$$

To obtain this scaling in the SPH model, we start with the expression for the pressure variance derived in Ref. 10

$$\langle \delta P^2 \rangle = \frac{\rho_{eq} k_B T c^2}{\Delta V}, \tag{41}$$

where δP is the fluctuation of pressure around the mean pressure. Noting that in the preceding equation $\Delta V = 1/n_{eq}$, $\delta P = c^2 m_0 \delta n$ (δn is the fluctuation of density around n_{eq}), and $\rho_{eq} = m_0 n_{eq}$, we obtain the scaling law for the speed of sound

$$c = \beta\sqrt{\frac{2h^3 \rho_{eq} T^*}{m_0^2}}, \tag{42}$$

where β is the inverse of the coefficient of variation of the particle number density,

$$\beta = \frac{n_{eq}}{\sqrt{\langle \delta n^2 \rangle}}. \tag{43}$$

This results in the EOS

$$P_i = T^* 2h^3 n_{eq} n_i \beta^2. \tag{44}$$

We numerically determined that to recover the correct hydrodynamic behavior, β^2 should be approximately equal to 5.5/2. A significantly smaller β^2 results in high compressibility of the fluid and may lead to numerical instability. For higher β (i.e., for less-compressible fluids), the thermodynamic variables become dependent on the speed of sound. Therefore, in all of our simulations, we set $\beta^2 = 5.5/2$. Figure 2 shows T^*_{kin}/T^* for $T^* = 0.001, 0.005, 0.01, 0.05$. For

all considered temperatures, convergence is reached at a number density of about $n_{eq} = 20$ with the error being less than 2%. Kinetic temperatures obtained from simulations using an SDPD implementation of the stochastic force are slightly higher with a maximum error of about 4%.

It follows from Eq. (39) that for all SPH particles having the same masses $m_i = m_0 = \rho_0/n_{eq}$, the velocity variance $\sigma_v^2 = \frac{1}{3}\sum_{i=1}^{N}(\delta v_{x,i}^2 + \delta v_{y,i}^2 + \delta v_{z,i}^2)$ should scale as

$$\sigma_v^2 = \frac{T^*}{m_0} = \frac{n_{eq}T^*}{\rho_0}, \tag{45}$$

i.e., for a fluid with a given mass density ρ_0, the velocity variance is inversely proportional to the mass of the SPH particles or linearly proportional to the resolution n_{eq}.

B. Spatial statistics of hydrodynamics variables

Here, we further validate the SPH model for LLNS equations by comparing statistics of pressure and velocity obtained from SPH simulations and analytical solutions.

Combining $\langle \delta P^2 \rangle = m_0 n_{eq} T^* c^2 n_{eq}$ and Eq. (40) leads to the scaling law for the pressure variance

$$\langle \delta P^2 \rangle \sim h^3 n_{eq}^3 T^{*2}. \tag{46}$$

Figure 3 plots $\langle \delta P^2 \rangle = \frac{1}{N}\sum_{i=1}^{N}(P_i - \langle P \rangle)^2$ (where $\langle P \rangle = \frac{1}{N}\sum_{i=1}^{N} P_i$) as a function of n_{eq} and for all prescribed T^*. It can be seen that $\langle \delta P^2 \rangle$ correctly scales as n^3 (or $1/m_0^3$) for the considered range of number densities and temperatures. Figure 4 shows the correlation function of the pressure fluctuations, $\langle \delta P(\mathbf{r}_i)\delta P(\mathbf{r}_j)\rangle / \langle \delta P^2 \rangle$, as a function of $r_{ij} = |\mathbf{r}_i - \mathbf{r}_j|$, obtained from the SPH simulations. The computed pressure correlation function agrees well with the theoretical expression[12]

$$\frac{\langle \delta P(\mathbf{r}_i)\delta P(\mathbf{r}_j)\rangle}{\langle \delta P^2 \rangle} = \delta_{ij}. \tag{47}$$

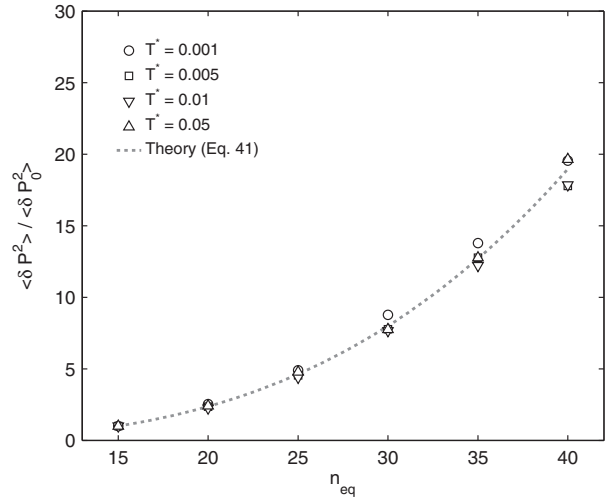

FIG. 3. Scaling of the pressure variance. $\langle \delta P_0^2 \rangle$ is obtained at $n_{eq} = 15$.

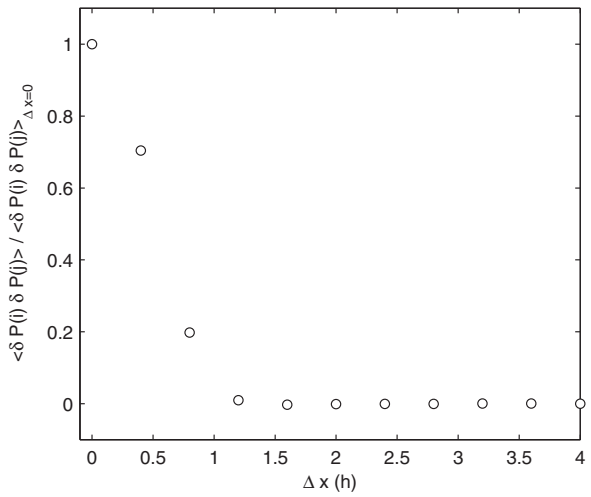

FIG. 4. Spatial correlation of pressure fluctuations. $T^* = 0.05$, $n_{eq} = 27$, $\rho_0 = 30$.

Due to the "smoothing" nature of the SPH interpolant (Eq. (14)), the unit peak in the correlation function at $r_{ij} = 0$ is diffused over the $0 \le r_{ij} \le h$ region. However, the correlation function correctly vanishes for $r_{ij} > h$.

The theoretical form of the velocity correlation and cross-correlation functions is given by Ref. 12 as

$$\langle \delta v_k(\mathbf{r}_i)\delta v_k(\mathbf{r}_j)\rangle = \langle \delta v_k^2 \rangle \delta_{ij} \tag{48}$$

and

$$\langle \delta v_k(\mathbf{r}_i)\delta v_l(\mathbf{r}_j)\rangle = 0 \quad k \neq l, \tag{49}$$

where v_k $(k = 1, 2, 3)$ is the k-component of the velocity vector. Figure 5 shows the spatial cross-correlation function of the velocity components v_x and v_y, which behave entirely uncorrelated as expected from Eq. (49). The spatial correlation function of velocity $\langle \delta v_x(\mathbf{r}_i)\delta v_x(\mathbf{r}_j)\rangle$ shown in Fig. 6 exhibits the same behavior as the pressure correlation function, i.e., we obtain a correct peak value for $r_{ij} = 0$ and a vanishing correlation function for $r_{ij} > h, h$. Although not shown here,

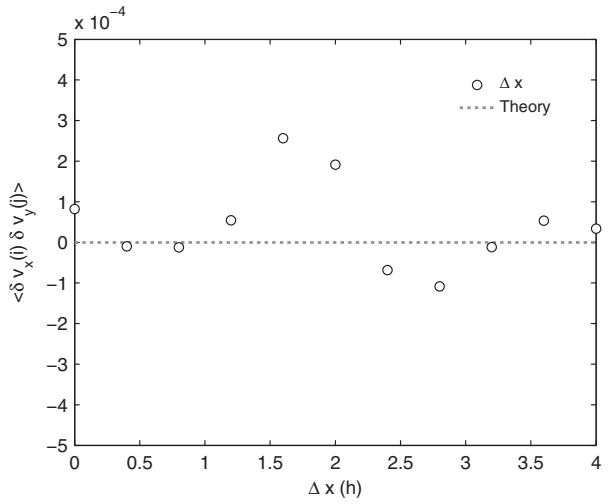

FIG. 5. Correlation of velocity components v_x and v_y.

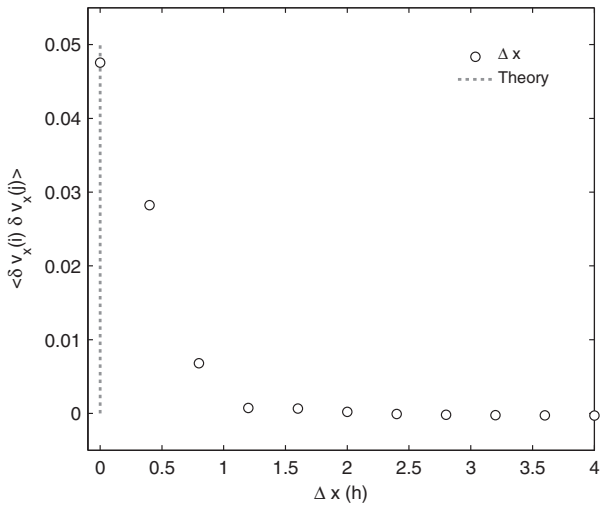

FIG. 6. Spatial correlation of velocity fluctuations.

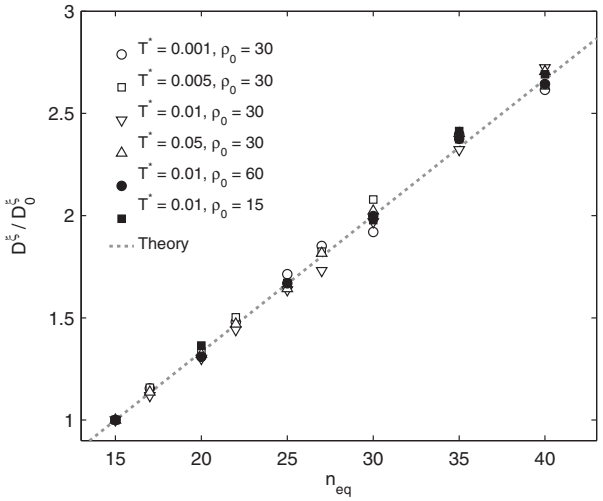

FIG. 7. Scaling of the stochastic diffusion coefficient with increasing resolution, where D_0^{ξ} is the diffusion coefficient at $n_{eq} = 15$ for each temperature T^*. D^{ξ} is obtained by linear regression of MSD/Δt where MSD $> 1.0\,h$.

the correlation function of the y and z components of velocity have the same correct behavior as shown in Fig. 6.

C. Self-diffusion coefficient

The coefficient of mechanical diffusion (describing the "diffusion" of the SPH particles), i.e., the self-diffusion coefficient, has a similar scaling behavior as the velocity variance. For example, for an SDPD model with a slightly different discretization of the viscous force than used in this work, the self-diffusion coefficient was obtained as[33]

$$D = \frac{\tau k_B T}{3} = \kappa \frac{n_{eq} h^2 \tilde{k}_B T}{\mu}, \tag{50}$$

with $\kappa = \frac{1}{12}$. For our SPH model, we numerically determined the value of $\kappa = 0.045$.

To validate the scaling of D, we compute the diffusion coefficient from SPH simulations over the same range of number densities and temperatures as in the previous example. The principal components of the diffusion tensor D_{ll}, $l = 1, 2, 3$ are obtained from the expression

$$\frac{dI_{ll}}{dt} = 2D_{ll}, \tag{51}$$

and the diffusion coefficient is calculated as

$$D = \frac{1}{3}\sum_{l=1}^{3} D_{ll}. \tag{52}$$

Here, the first and second moments of the particle displacements in l direction are computed as

$$I_l(t) = \sum_{i}^{N} \left(x_{l,i} - x_{l,i}^0\right)/N \tag{53}$$

and

$$I_{ll}(t) = \sum_{i}^{N} I_{ll} - \left(x_{l,i} - x_{l,i}^0\right)^2/N, \tag{54}$$

where N is the total number of particles and x^0 denotes the initial particle position.

Figure 7 shows the resulting scaling of the diffusion coefficients with changing resolution, which agrees with Eq. (50).

The same correct linear scaling for the diffusion coefficient is obtained for the whole temperature range considered in the simulations (see Fig. 8).

The corresponding Schmidt numbers for all simulations are shown in Fig. 9.

VI. SPH MODEL FOR HIGHLY DILUTED SOLUTIONS

Here, we examine the enhancement of Fickian diffusion by thermal fluctuations in non-equilibrium systems. In this section, we study highly diluted solutions, i.e., we assume that the density of the solution (hence, the mass of the SPH particles) does not depend on the concentration

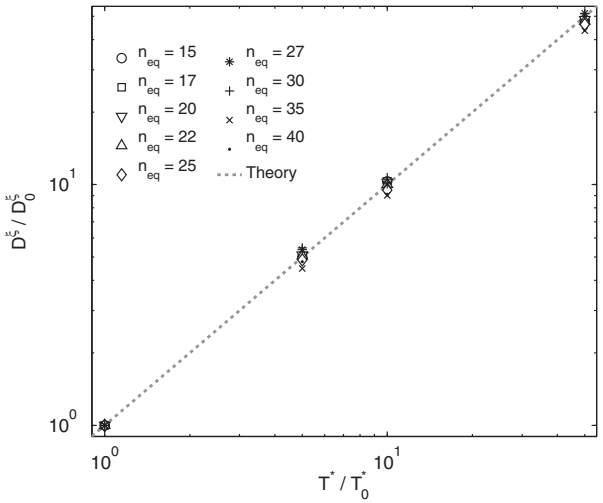

FIG. 8. Scaling of the stochastic diffusion coefficient with increasing temperature T^*. Here, $T^* = 0.001, 0.005, 0.01, 0.05$ ($T_0^* = 0.001$), and D_0^{ξ} corresponds to the diffusion coefficient at $T^* = 0.001$ for each number density n_{eq}. The diffusion coefficient D^{ξ} is obtained by linear regression of MSD/Δt where MSD $> 1.0\,h$.

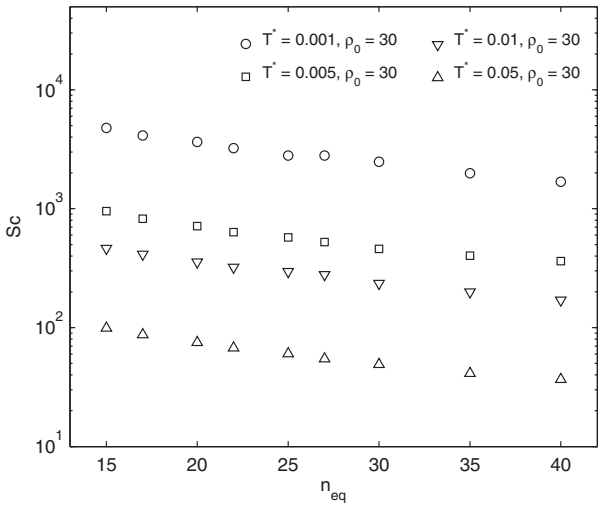

FIG. 9. Schmidt numbers Sc determined from the simulations.

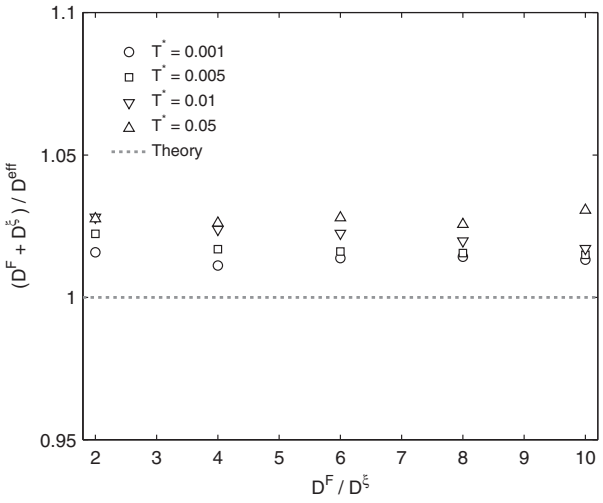

FIG. 10. Accuracy of the diffusion enhancement for different ratios of D^F/D^ξ. Diffusion coefficients $D^\xi + D^F$ are obtained from simulations where only Fickian diffusion is active or only thermal fluctuations occur and then are compared to simulations where both are present.

(mass fraction) of the solution, C. As shown numerically in Refs. 13 and 21, the effective diffusion coefficient D^{eff} consists of a deterministic Fickian part D^F and a stochastic contribution D^ξ: $D^{eff} = D^F + D^\xi$. In turn, D^ξ is a result of the random advection (which is characterized by the self-diffusion coefficient in Eq. (50)) and the random flux $\boldsymbol{J}$ in the stochastic advection-diffusion equation.

To study the effect of diffusion enhancement, we simulate a spherical plume with radius $3\,h$ and an initial uniform concentration $C_0 = 1.0$ surrounded by a solution with zero concentration. A periodic domain with the dimensions $L_x = L_y = L_z = 16\,h$ is used in this study. The SPH particles are initially placed on a regular grid. The initial number density in these simulations is $n_{eq} = 27$, the viscosity is $\mu = 10$, and the mass density of the solvent is $\rho_0 = 30.0$, such that the mass of solvent carried by particle i is $m_i = \rho_0/n_{eq} = 1.11$. We run the simulations with four different temperatures ($T^* = 0.001$, 0.005, 0.01, and 0.05), the ratio D^F/D^ξ ranges from 2 to 10, and the value of D^ξ is estimated from Eq. (50).

The resulting diffusion coefficient is determined from simulations as $D^{eff} = \frac{1}{3}(D_{11}^{eff} + D_{22}^{eff} + D_{33}^{eff})$, where D_{ll}^{eff} is found as

$$\frac{dI_{ll}}{dt} = 2D_{ll}^{eff}. \tag{55}$$

The second moments of the plume in l direction are calculated as

$$I_{ll} = \frac{1}{M}\sum_i (x_{l,i} - I_l)^2 C_i m_i, \tag{56}$$

the first moments are found as

$$I_l = \frac{1}{M}\sum_i x_{l,i} C_i m_i, \tag{57}$$

and the total mass of the solute is

$$M = \sum_i C_i m_i. \tag{58}$$

To analyze the accuracy of the SPH solution of the stochastic and deterministic advection-diffusion equations, we solve: (1) the deterministic diffusion equation in the absence of advection, (2) the coupled LLNS and stochastic advection equation ($D^F = 0$), and (3) the coupled LLNS and stochastic advection-diffusion equations. In the first case, we compute the resulting diffusion coefficient and compare it with the prescribed Fickian diffusion coefficient. In the second case, we numerically compute D^ξ. Once the deterministic solution is verified and D^ξ is evaluated, we compute the effective diffusion coefficient in the third simulation as

$$D^{eff} = D^\xi + D^F \tag{59}$$

and compare this value with the effective diffusion coefficient obtained from the SPH solution of the LLNS and stochastic diffusion equation with the corresponding D^F and T^*.

The results of the simulations indicate a very good agreement between D^{eff} obtained from Eq. (59) and the solution of the full stochastic diffusion equation (see Fig. 10). The relative errors are between 0.8% and 2.5%.

Figure 11 shows a cross section of the spherical plume for three different ratios of $D^F/D^\xi = 2, 4, 8$ at time $t = 2$, 20, 40 and a temperature of $T^* = 0.01$. Results demonstrate that for rather high ratios of D^ξ/D^F—that is, a mesoscopic scale where the microscopic effects begin to dominate the transport description—the concentration front is characterized by clear fluctuations (e.g., upper right panel in Fig. 11). In contrast, for a lower ratio of D^ξ/D^F, this effect is less pronounced as the time evolution of the concentration front is controlled by the Fickian description of diffusive transport.

VII. SPH SOLUTION OF THE COUPLED LLNS AND STOCHASTIC DIFFUSION EQUATIONS

Here, we use the coupled stochastic SPH model to study the effect of gravity on thermally enhanced diffusive transport. Specifically, we analyze perturbations of a front between

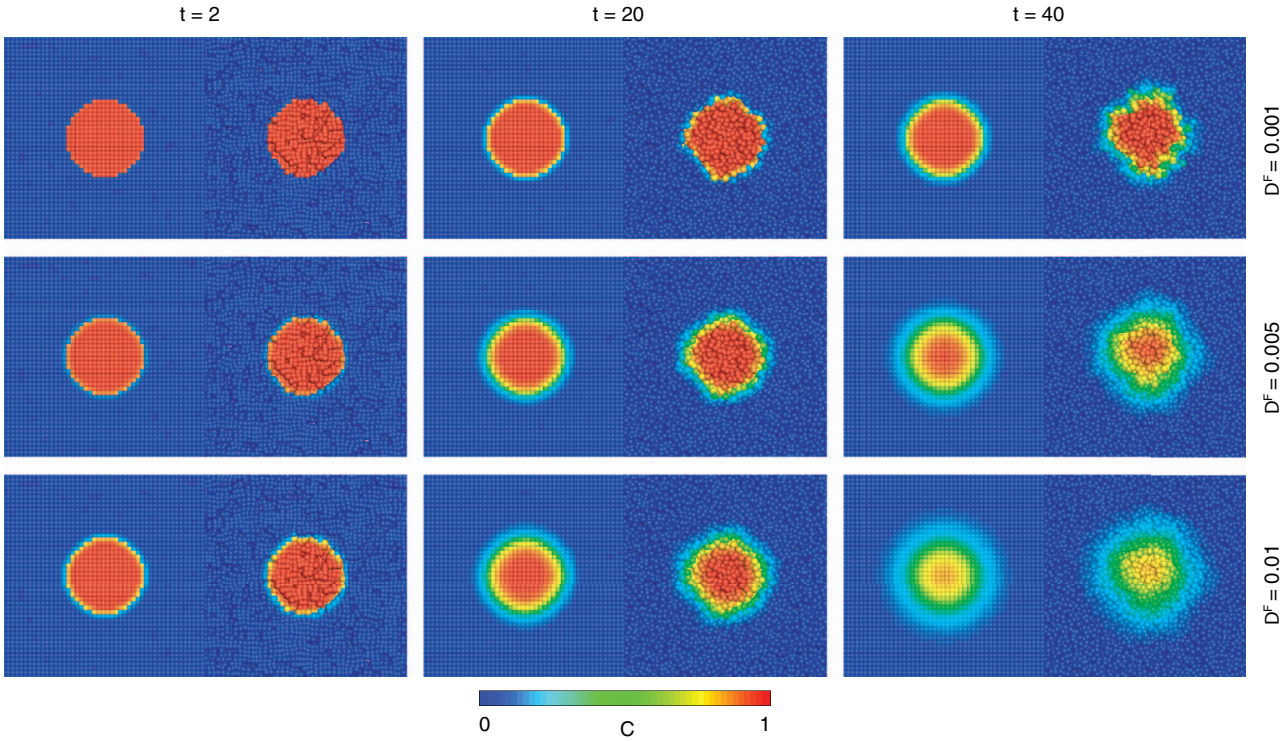

FIG. 11. Cross section of spherical plumes at times $t = 2$, 20, 40 and at a temperature of $T^* = 0.01$. Left picture at each time corresponds to pure Fickian diffusion, right side to Fickian diffusion enhanced by thermal fluctuations at the given temperature. $D^F/D^\xi = 2, 4, 8$ for $D^F = 0.001, 0.005, 0.01$, i.e., the impact of thermal fluctuations on the concentration field decreases from top to bottom. Cubic domain with edge size $16\,h$ with an initial plume diameter of $6\,h$.

two miscible fluids due to random stresses and fluxes in the momentum and advection-diffusion equations. In the coupled model, we solve the LLNS and stochastic advection-diffusion equations with the mass of SPH particles (and density of the solution) depending on C, according to Eq. (23).

We simulate a three-dimensional domain filled with the solution of a conservative species C. We consider two cases: (1) initial C is zero in the upper half of the domain and one in the lower half of the domain, and (2) initial C is one in the upper half of the domain and zero in the lower half of the domain. In the first case, the fluid configuration is stable, i.e., the initially sharp front widens due to molecular diffusion and perturbs due to random fluctuations in fluid velocity and diffusive fluxes. In this case, we use the SPH model to study how gravity suppresses perturbations of the front (also known as giant fluctuations). In the second case, the flow configuration is unstable as the heavy fluid on top tries to replace the light fluid on the bottom, a phenomenon known as the Rayleigh-Taylor instability. In this case, we use the stochastic SPH model to study the effect of random stresses and diffusive fluxes on the development of the Rayleigh-Taylor instability.

In both study cases, the domain size is $L_x = L_y = 16\,h$ and $L_z = 8\,h$. The upper and lower horizontal boundaries are assumed to be impermeable, and all of the vertical boundaries are treated as periodic. To impose no-flow boundary conditions at the bottom of the domain, we set a layer of immobile particles with the thickness $\Delta L_z = 1\,h$. Particles in this layer contribute to the density evolution and forces in the LLNS equations (i.e., the summations in Eqs. (17) and (16) are over all fluid and boundary particles). In addition, a bounce-back condition is used to implement the no-flow boundary condition. The bounce-back boundary condition is implemented by inverting the velocity vector of particles crossing the impermeable boundary ($z_i < 1\,h$ or $z_i > 16\,h$) and returning these particles into the fluid domain along their "exit" trajectories. The zero-flux boundary condition for the stochastic advection-diffusion equation is imposed by including only fluid particles in the summations in Eq. (24). The solvent mass of all particles is set to $m_i^0 = m_0 = 1$, and m_i is computed according to Eq. (23). The parameter κ in Eq. (23) is related to the Atwood number, A, via

$$A = \frac{m(C=1) - m(C=0)}{m(C=1) + m(C=0)} = \frac{\kappa}{2m^0 + \kappa}, \qquad (60)$$

where $m(C=1)$ and $m(C=0)$ are the masses of particles with $C = 1$ and $C = 0$, respectively.

A. Giant fluctuations

Here, we consider two scenarios: (1) with gravity and (2) in the absence of gravity. In both scenarios, the solution with $C = 0$ ("light fluid") lies on top of the solution with $C = 1$ ("heavy fluid"), the Atwood number is $At = 0.83$ ($\kappa = 10$), and the temperature is set to $T^* = 0.001$. In the first scenario, the system is initially equilibrated, i.e., brought to hydrostatic condition by solving only the NS equations. During the equilibration process, $C = 0$ and 1 are maintained in the upper and lower part of the domain, respectively. In the absence of gravity, there is no need to pre-equilibrate the particle system in the simulations of the second scenario. For

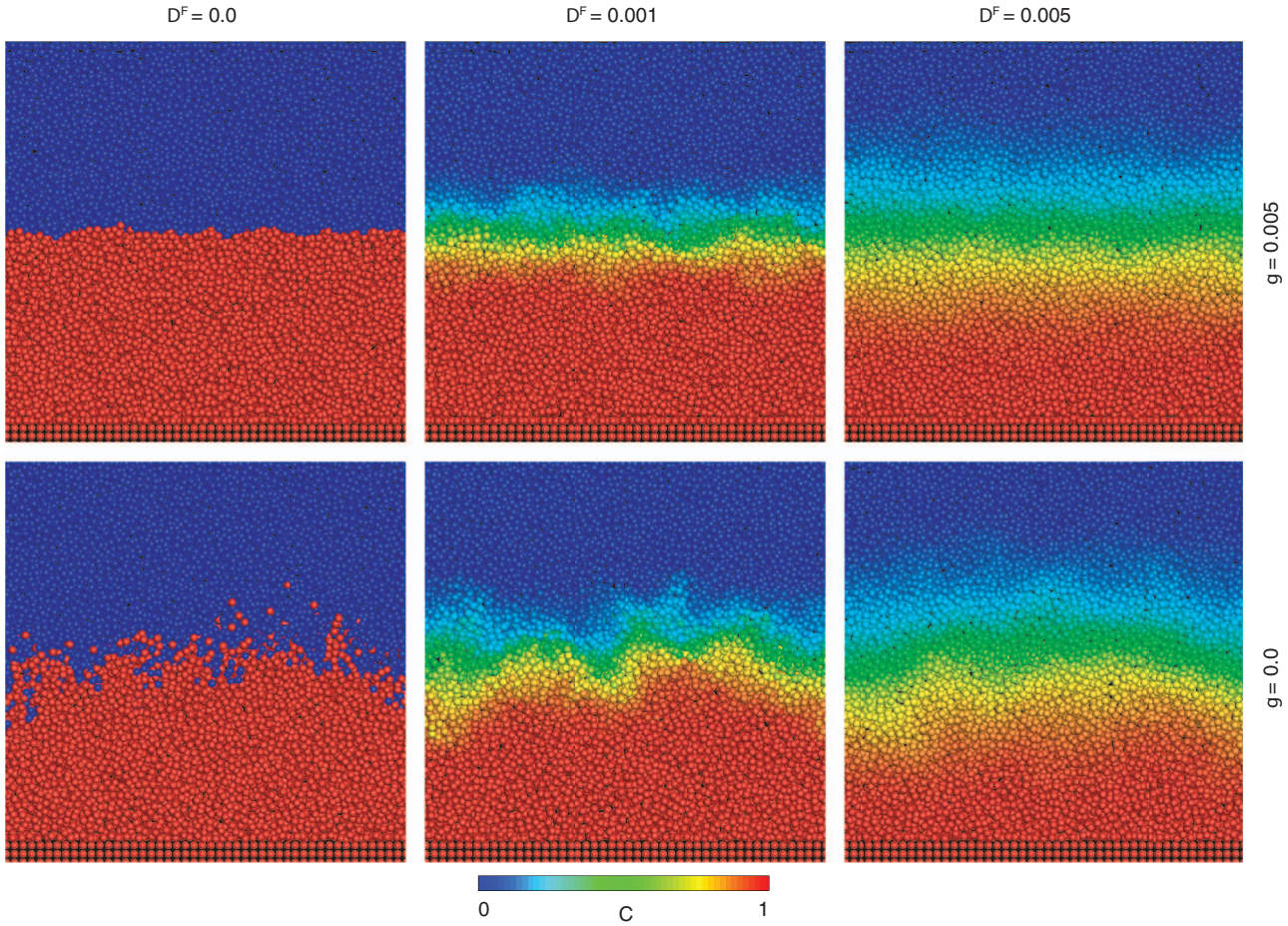

FIG. 12. Cross section of the interface between a heavy fluid and a light fluid on top at time $t = 414$. Temperature is $T^* = 0.001$, $\kappa = 10$, $\mu = 10$. (Upper row) In the presence of gravity with same increase of Fickian diffusion from left to right. (Lower row) Without gravity and increasing Fickian diffusion from left to right.

each scenario, we conduct three simulations: (1) no Fickian diffusion, i.e., $D^F = 0.0$; (2) $D^F = 0.001$; and (3) $D^F = 0.005$.

Figure 12 shows the cross sections of the resulting concentrations at time $t = 414$ for each of the six simulations described. Subfigures in the top row show the distribution of C obtained from the simulations in the absence of gravity, where the presence of giant fluctuations or perturbations of the front is clear. Subfigures in the bottom row show the distribution of C obtained from the simulations with gravity. It is evident that gravity significantly reduces front perturbations for all considered values of D^F, but the effect of gravity becomes less pronounced with increasing D^F. As D^F becomes significantly larger than D^ξ (or when $T^* \to 0$), the stochastic diffusion reduces to a deterministic diffusion, and fluctuations completely disappear.

1. Structure factor

To analyze the diffusive interface, we decompose the two-dimensional concentration field into its Fourier modes and wave vectors q to obtain a one-dimensional, radially averaged, static power spectrum $\boldsymbol{S}(q)$.[34] We remap the original particle data onto a regular grid with $L_xR \times L_yR$ cells by averaging the particle concentration $\boldsymbol{C}(x, y, z)$ of all particles in each cell over the depth L_z, excluding the lower boundaries, to create a two-dimensional concentration field $\boldsymbol{C}(x, y)$ normal to z (see Fig. 14). Here, $R = 1$ is chosen to minimize interpolation errors due to the resampling and $L_xR = L_yR = N_x = N_y = N$. The averaging of the particle concentrations can be understood as a numerical equivalent of the common experimental shadowgraphy technique.[4,35] We follow the work of Refs. 4 and 36 and obtain the static power spectrum from the relative concentration $\boldsymbol{C}^*(x, y) = [\boldsymbol{C}(x, y) - \boldsymbol{C}_0(x, y)]/\boldsymbol{C}_0(x, y)$, where $\boldsymbol{C}_0(x, y)$ denotes the initial concentration. To convert the two-dimensional Fourier transform

$$\boldsymbol{F}(q_x, q_y) = \sum_{x=0}^{N_x-1} \sum_{y=0}^{N_y-1} \boldsymbol{C}^*(x, y) e^{-i2\pi(q_x x/N_x + q_y y/N_y)} \quad (61)$$

and its complex result $\boldsymbol{F}(q_x, q_y)$ into a one-dimensional equivalent, we first construct a two-dimensional power spectrum $\boldsymbol{S}(q_x, q_y) = |\Re[\boldsymbol{F}(q_x, q_y)]|^2$, where $\Re$ denotes the real parts of $\boldsymbol{F}$ and the first and third (second and fourth) quadrants of the field $\boldsymbol{F}$ have been swapped to relocate the lowest spatial frequencies q_x and q_y to the center.

We then rotate a sampling profile line with endpoints $\boldsymbol{P}_a$ and $\boldsymbol{P}_b$ about the center coordinate $\boldsymbol{P}_a = (N/2 = 0,$

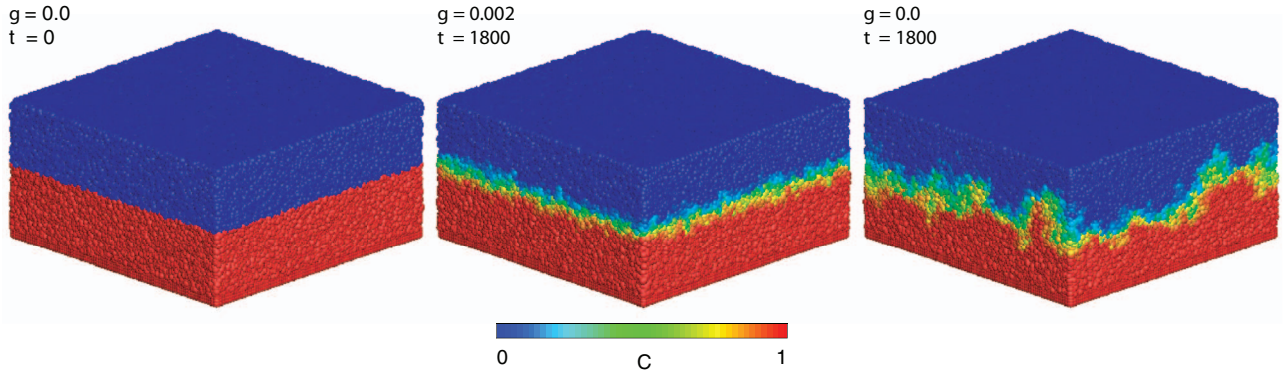

FIG. 13. Concentration fields $\boldsymbol{C}(x, y, z)$ at $t = 0$ and $t = 1800$ with gravity (middle) and without gravity (right) at a temperature of $T^* = 0.003$.

$N/2 = 0$) in 1° increments, where

$$\boldsymbol{P_b} = \frac{N}{2}(1 + \boldsymbol{u}) \qquad \boldsymbol{u} = (\cos(\theta), \sin(\theta)), \tag{62}$$

and compute power spectrum profiles $\boldsymbol{S}^{\theta}_{ab}(q) = q$ between $\boldsymbol{P}_a$ and $\boldsymbol{P}_b$ to obtain the one-dimensional radially averaged power spectrum $\boldsymbol{S}(q) = \frac{1}{360}\sum_{\theta=0}^{\theta=2\pi} \boldsymbol{S}_{ab}$.

In the absence of gravity, the nonequilibrium concentration fluctuations are known to exhibit a characteristic q^{-4} decay of the power spectrum.[37] However, this can only be observed over a limited range of wavenumbers due to several effects that relax the fluctuations and eliminate the scale-invariant character. At low wavenumbers, the primary reason is a finite size of the domain.[35] Gravity dampens the fluctuations, leading to a much weaker dependence of the power spectrum on wavenumber.[36]

We obtain the power spectrum $\boldsymbol{S}(q)$ from simulations similar to the ones described in Sec. VII with the domain size $L_x = L_y = 32\,h$ and $L_z = 16\,h$, temperature $T^* = 0.003$ (which corresponds to a Schmidt number of $Sc \approx 1000$), and $\kappa = 10$. In these simulations, the light fluid ($C = 0$) lies on top of the heavy fluid ($C = 1$). According to Refs. 36 and 38, in the absence of gravity, the scale-invariant characteristics of the power spectrum are independent of the fluid configuration and concentration gradient and scale as

$$S(q)/S^{\infty} = (q^4 + Bq^2 + \Lambda^4)^{-1}. \tag{63}$$

Here, $B = \Lambda\tanh(\Lambda/2)[2\Lambda\tanh(\Lambda/2) - 4]$, and Λ is a fitting constant. To normalize the data, the asymptotic value of $S^{\infty} = \lim_{q\to\infty} S(q)q^4$ is obtained from a fit of the linear part of $S(q)q^4$, which corresponds to fitting a power law function $S^{\infty}q^{-4}$ to $S(q)$.

Figure 13(a) shows the initial concentration distribution, and Figs. 13(b) and 13(c) show the concentration distribution at time $t = 1800$ with and without gravity, respectively. Figure 14 depicts the corresponding remapped two-dimensional concentration fields $\boldsymbol{C}^*(x, y)$ used to obtain the power spectra. Figure 15 shows the resulting power spectra scaled onto the universal curve according to Eq. (63) with $\Lambda = 2.33$ and the theoretical scaling for bounded and unbounded conditions. This confirms the scale-invariant nature of the fluctuation front and the saturation due to finite-size effects at low wavenumbers. The power spectrum of the interface in the presence of gravity clearly shows the saturation of the divergence at low wavenumbers. It should be noted, that even when gravity relaxes the interface fluctuations, the theory also predicts a q^{-4} divergence at very high wavenumbers,[36] which is only weakly visible in our simulations. It is believed this is an effect of insufficient resolution, and simulations with $n_{eq} > 27$ may be necessary to properly resolve the divergence.

B. Rayleigh-Taylor instability

Here, we examine the effect of thermal fluctuations on the development of the Rayleigh-Taylor instability, an unstable displacement of a light ($C = 0$) fluid with a heavy fluid ($C = 1$) under the action of gravity. In the considered cases, the Atwood number is $A = 0.6$ ($\kappa = 3$), gravity is $g = 0.002$, viscosity is $\mu = 10$, and the number density is $n_{eq} = 27$. The domain size is $L_x = 16\,h$, $L_y = 8\,h$, and $L_z = 32\,h$. The no-flow boundary condition is imposed in the z direction by placing a layer of boundary particles at the bottom of the domain. Periodic boundary conditions are imposed in the x and y directions. To initiate the Rayleigh-Taylor instability, we perturb the interface according to

$$z(x) = z_0 + cos(\pi x/L_x)\eta_0, \tag{64}$$

where $z_0 = 0.5L_z + 1$ with the initial amplitude $\eta_0 = 0.5$ and the wavelength $\lambda = 16\,h$.

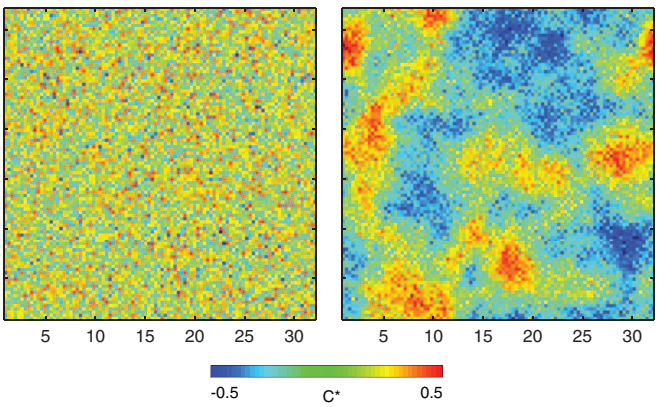

FIG. 14. Two-dimensional concentration fields $\boldsymbol{C}^*(x, y)$ with $R = n^{1/3}$ at $t = 1800$ with gravity (left) and without gravity (right).

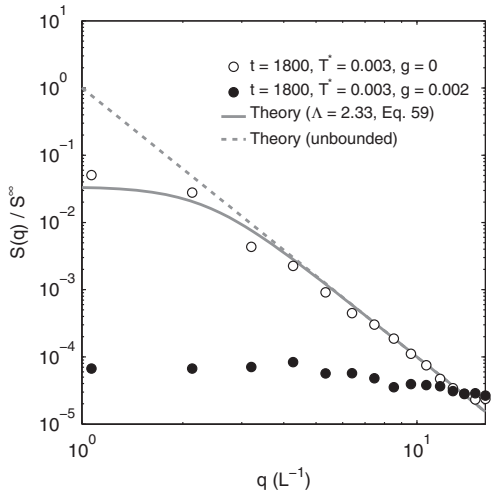

FIG. 15. Power spectra obtained from the remapped concentration fields at $t = 1800$, including the effect of gravity. Due to resolution limitations, the simulations with gravity do not show a fully developed q^{-4} divergence, which would be expected only for very high wavenumbers. Thus, the value of S^{∞} is obtained from a fit of $S(q)q^4$ in the same range as for $g = 0.0$.

This yields a pseudo-two-dimensional setup. To bring the system to a hydrostatic equilibrium, we solve the LLNS equations, including thermal fluctuations (no Fickian diffusion), and constantly reassign the appropriate concentrations above and below the interface defined by Eq. (64). In the final simulations, we investigate three cases with the same effective diffusion coefficient $D^{eff} = 0.00036$ ($Sc \approx 1000$): (1) $D^{\xi} = 0.00012$, $D^{F} = 0.00024$; (2) $D^{\xi} = 0$, $D^{F} = 0.00036$; and (3) $D^{\xi} = 0.00012$, $D^{F} = 0.00024$ (SDPD implementation of the stress tensor, see Eq. (37)) to compare the time evolution of the diffusive interface.

After Ref. 39, the amplitude of the interface has to satisfy

$$\frac{d\eta}{dt} = \eta n(A, \nu, k), \tag{65}$$

where η is the amplitude of the diffusive interface and n is exponential growth coefficient given by Refs. 39–41

$$n = \sqrt{A\frac{gk}{\psi(a, A) + \nu^2 k^4}} - (\nu + D^{eff})k^2. \tag{66}$$

Here, $\nu = (\mu_1 + \mu_2)/(\rho_1 + \rho_2)$ is the kinematic viscosity, k is the wavenumber of the perturbed interface, $a = (2k\sqrt{D^{eff}t})^{-1}$, and $\psi = 1 + \sqrt{2/\pi}a^{-1}$ for $a \geq 1$. Consequently, the time-dependent solution is

$$\eta(t) = \eta_0 \exp\left(t\left[\sqrt{A\frac{gk}{\psi(a, A)} + k^4\nu} - k^2\nu - D^{eff}k^2\right]\right). \tag{67}$$

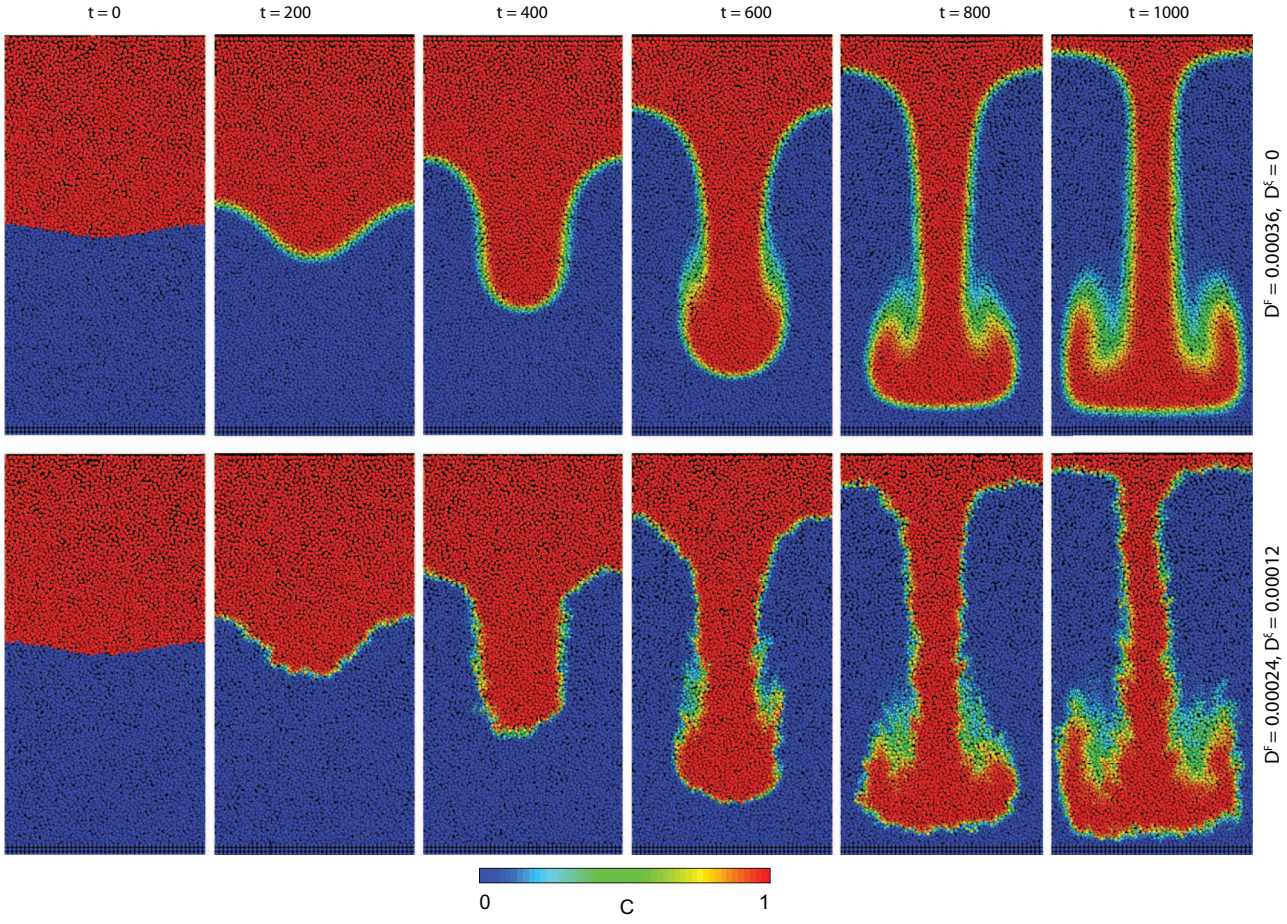

FIG. 16. Rayleigh-Taylor instability at a Schmidt number of $Sc \approx 1000$ ($D^{eff} = 0.00036$), $At = 0.6$ ($\kappa = 3$), gravity $g = 0.002$, viscosity $\mu = 10$, and number density $n_{eq} = 27$. Domain size is $L_x = 16\,h$, $L_y = 8\,h$, and $L_z = 32\,h$. (Upper row) Only Fickian diffusion with $D^{F} = 0.00036$. (Lower row) $D^{F} = 0.00024$ and $D^{\xi} = 0.00012$, $T^{*} = 0.002$.

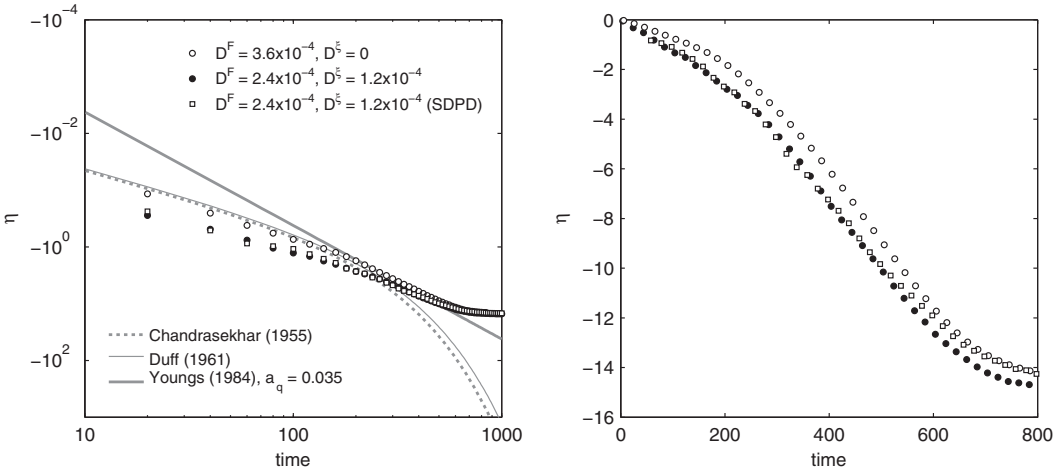

FIG. 17. (Left) Simulations of the Rayleigh-Taylor instability with same effective diffusion $D^{eff} = 0.00036$ at Schmidt number $Sc \approx 1000$ and $g = 0.002$ and the corresponding simulations using the SDPD implementation. The solution of Refs. 43 and 39 have been derived for early times. In contrast, the analytical solution of Ref. 47 is valid for late times and employs the α_q calibration parameter, which has been reported by various laboratory and numerical experiments to exist in a range between 0.01 and 0.08[53] (here $a_q = 0.035$). (Right) Same simulations plotted on linear scale.

A simpler form neglecting the effect of viscosity and diffusion is given as[42–44]

$$\eta(t) = \eta_0 \exp\left(t\sqrt{Agk}\right). \tag{68}$$

It should be noted that Eqs. (67) and (68) are only valid at early times and/or small η because these equations have been derived from the linearized hydrodynamic equations.[45] At later times (when $\eta \approx \lambda/2\pi$[46]), departure from the exponential time dependence to a more complex quadratic time dependence[47,48]

$$\eta(t) = \alpha_q A g t^2 \tag{69}$$

and finally to a linear evolution of the diffusive front has been observed.[49–52]

Figure 16 shows the resulting evolution of the unstable front, and Fig. 17 displays the corresponding interface amplitude for both the stochastic and deterministic cases. Note that the interface position at each time step has been approximated by averaging the lowest particle position that satisfies $(0.5 - C) \leq 0$ and $Lx/2 - 0.5h > x < Lx/2 + 0.5h$ between 0 and L_y with $\Delta y = 0.25h$. In general, both solutions agree well with the analytical solutions of Refs. 43 and 39 for early times ($t \lesssim 300$) and with the late time behavior given by Ref. 47 ($t \gtrsim 300$), where $a_q = 0.035$. This is in agreement with the wide range of a_q values that have been reported in literature[53] and are between 0.01 and 0.08. Figure 17 (right panel) shows that the front in the stochastic simulation propagates faster, especially at late times. The rate of the front perturbation growth is proportional to the concentration gradient. The coefficient of Fickian diffusion is smaller in the stochastic model ($D^F < D^{eff}$) than in the deterministic model ($D^F = D^{eff}$), and as a result, the concentration gradients across the interface are higher in the stochastic simulation than in the deterministic simulation, which can be seen in Fig. 16. Therefore, the front perturbation grows faster in the stochastic simulation than in the deterministic simulation. Simulations using the SDPD implementation display a slightly slower development of the front growth at late times compared to the LLNS-SPH simulations. This is most likely caused by the difference in kinetic temperatures (about 4%, see Fig. 2) as development of vortices rolled up along the tail is favored, leading to higher drag forces on the perturbation front at late times.

VIII. CONCLUSION

We presented a novel, SPH-based method for solving coupled LLNS and stochastic advection-diffusion equations. It is shown that the resulting stochastic SPH model produces a correct scaling behavior of thermodynamic quantities, such as velocity variance and self-diffusion coefficient, and the right spatial correlation of pressure and velocities. We used the SPH model to investigate the effect of thermal fluctuations on diffusive mixing. First, we simulated diffusion of a plume and demonstrated the accuracy of the SPH model with an error of less than 2%. Then, the role of thermal fluctuations on the evolution of a diffusive interface between a light fluid lying on top of a heavy fluid has been demonstrated. In agreement with recent laboratory experiments and theoretical considerations, we demonstrated that in the absence of gravity, the SPH model recovers the characteristic q^{-4} divergence of the interface power spectrum and its scale-invariant nature. Also in agreement with previous studies, our results show that gravity reduces perturbations of the miscible front. Finally, we used the stochastic SPH model to study the effect of thermal fluctuations on the development of the Rayleigh-Taylor instability. We found that random thermal fluctuations slightly accelerate the development of the instability. In the stochastic SPH model, mixing of two miscible fluids results from mechanical mixing of two fluids due to random advection and diffusive mixing. In the standard deterministic description (based on the NS and advection-diffusion equations), the mixing is treated as an effective diffusion process. Therefore, the deterministic model produces smaller concentration gradients across the front separating two miscible fluids, which slows the development of the Rayleigh-Taylor instability. The evolution of the miscible front, obtained from the deterministic

and stochastic models, agrees well with the analytical solutions, which demonstrated the SPH model's accuracy.

ACKNOWLEDGMENTS

This work was partially supported by the DAAD (German Academic Exchange Service) providing J. Kordilla with an international research scholarship at Pacific Northwest National Laboratory (PNNL), USA. A. M. Tartakovsky and W. Pan were supported by the Applied Mathematics Program within the U.S. Department of Energy (DOE) Office of Advanced Scientific Computing Research (ASCR) and PNNL. A portion of this work was made possible by the CM4: Collaboratory on Mathematics for Mesoscopic Modeling of Materials. PNNL is operated by Battelle for the DOE under Contract DE-AC05-76RL01830.

[1]E. Cussler, *Diffusion: Mass Transfer in Fluid Systems* (Cambridge University Press, 1997).
[2]J. Bear, *Dynamics of Fluids in Porous Media* (Courier Dover Publications, 1972).
[3]A. Fick, Ann. Phys. **170**, 59 (1855).
[4]D. Brogioli, A. Vailati, and M. Giglio, J. Phys.: Condens. Matter **12**, A39 (2000).
[5]A. Vailati and M. Giglio, Nature (London) **390**, 4 (1997).
[6]F. Croccolo, D. Brogioli, A. Vailati, M. Giglio, and D. S. Cannell, Phys. Rev. E **76**, 041112 (2007).
[7]A. Einstein, Ann. Phys. **322**, 549 (1905).
[8]M. von Smoluchowski, Ann. Phys. **326**, 756 (1906).
[9]H. Callen and T. Welton, Phys. Rev. **83**, 34 (1951).
[10]L. D. Landau and E. M. Lifshitz, *Fluid Mechanics, Course of Theoretical Physics Vol. 6* (Butterworth-Heinemann, 1987).
[11]M. Serrano and P. Español, Phys. Rev. E **64**, 046115 (2001).
[12]J. B. Bell, A. Garcia, and S. A. Williams, Phys. Rev. E **76**, 016708 (2007).
[13]A. Donev, J. B. Bell, A. de la Fuente, and A. Garcia, Phys. Rev. Lett. **106**, 204501 (2011).
[14]A. Donev and E. Vanden-Eijnden, Commun. Appl. Math. Comput. Sci. **5**, 149 (2010).
[15]A. Ladd, Phys. Rev. Lett. **70**, 1339 (1993).
[16]P. Español, M. Serrano, and H. Öttinger, Phys. Rev. Lett. **83**, 4542 (1999).
[17]P. Español and M. Revenga, Phys. Rev. E **67**, 026705 (2003).
[18]M. Grmela and H. Öttinger, Phys. Rev. E **56**, 6620 (1997).
[19]H. Öttinger and M. Grmela, Phys. Rev. E **56**, 6633 (1997).
[20]M. Serrano, G. Fabritiis, P. Español, E. Flekkøy, and P. Coveney, J. Phys. A **35**, 1605 (2002).
[21]A. Donev, J. B. Bell, A. de la Fuente, and A. L. Garcia, J. Stat. Mech.: Theory Exp. **2011**, P06014.
[22]J. J. Monaghan, SIAM J. Sci. Comput. **3**, 422 (1982).
[23]A. Tartakovsky and P. Meakin, J. Comput. Phys. **207**, 610 (2005).
[24]R. A. Gingold and J. J. Monaghan, J. Comput. Phys. **46**, 429 (1982).
[25]J. J. Monaghan, Rep. Prog. Phys. **68**, 1703 (2005).
[26]Y. I. Zhu and P. J. Fox, J. Comput. Phys. **182**, 622 (2002).
[27]J. P. Morris, J. Comput. Phys. **136**, 214 (1997).
[28]A. Tartakovsky and P. Meakin, Phys. Rev. E **72**, 026301 (2005).
[29]J. Kordilla, A. Tartakovsky, and T. Geyer, Adv. Water Resour. **59**, 1 (2013).
[30]J. J. Monaghan, Annu. Rev. Astron. Astrophys. **68**, 543 (1992).
[31]R. M. Füchslin, H. Fellermann, A. Eriksson, and H.-J. Ziock, J. Chem. Phys. **130**, 214102 (2009).
[32]M. Allen and D. Tildesley, *Computer Simulation of Liquids* (Clarendon Press, Oxford, 1989), p. 404.
[33]S. Litvinov, M. Ellero, X. Hu, and N. A. Adams, J. Chem. Phys. **130**, 021101 (2009).
[34]C. Redies, J. Hasenstein, and J. Denzler, Spatial Vis. **21**, 137 (2007).
[35]A. Vailati, R. Cerbino, S. Mazzoni, M. Giglio, G. Nikolaenko, C. J. Takacs, D. S. Cannell, W. V. Meyer, and A. E. Smart, Appl. Opt. **45**, 2155 (2006).
[36]A. Vailati, R. Cerbino, S. Mazzoni, C. J. Takacs, D. S. Cannell, and M. Giglio, Nat. Commun. **2**, 290 (2011).
[37]T. Kirkpatrick, E. Cohen, and J. Dorfman, Phys. Rev. A **26**, 995 (1982).
[38]J. M. Ortiz de Zárate, F. Peluso, and J. V. Sengers, Eur. Phys. J. E **15**, 319 (2004).
[39]R. E. Duff, F. H. Harlow, and C. W. Hirt, Phys. Fluids **5**, 417 (1962).
[40]R. Bellman and R. Pennington, Q. Appl. Math. **12**, 151 (1953).
[41]R. Hide, Proc. R. Soc. London, Ser. A **233**, 376 (1955).
[42]Lord Rayleigh, Proc. London Math. Soc. **14**, 170 (1883).
[43]S. Chandrasekhar, Math. Proc. Cambridge Philos. Soc. **51**, 162 (1955).
[44]G. Taylor, Proc. R. Soc. London, Ser. A **201**, 192 (1950).
[45]P. Vandervoort, Astrophys. J. **134**, 699 (1961).
[46] N. N. Anuchina, Yu. A. Kucherenko, V. E. Neuvazhaev, V. N. Ogibina, L. I. Shibarshov, and V. G. Yakovlev, Fluid Dyn. **13**, 916 (1979).
[47]D. L. Youngs, Physica D **12**, 32 (1984).
[48]K. Read, Physica D **12**, 45 (1984).
[49]D. Layzer, Astrophys. J. **122**, 1 (1955).
[50]P. Garabedian, Proc. R. Soc. London, Ser. A **241**, 423 (1957).
[51]G. Birkhoff and D. Carter, Indiana Univ. Math. J. **6**, 769 (1957).
[52]M.-A. Lafay, B. Le Creurer, and S. Gauthier, Europhys. Lett. **79**, 64002 (2007).
[53]J. Glimm, J. Grove, X. Li, W. Oh, and D. Sharp, J. Comput. Phys. **169**, 652 (2001).